

# Nanoscale

rsc.li/nanoscale



ISSN 2040-3372

**PAPER**

Soorathep Kheawhom *et al.*

Tailoring the MOF structure via ligand optimization afforded a dandelion flower like CoS/Co-N<sub>x</sub>/CoNi/NiS catalyst to enhance the ORR/OER in zinc-air batteries


 Cite this: *Nanoscale*, 2022, **14**, 17908

## Tailoring the MOF structure *via* ligand optimization afforded a dandelion flower like CoS/Co–N<sub>x</sub>/CoNi/NiS catalyst to enhance the ORR/OER in zinc–air batteries†

 Mohan Gopalakrishnan,<sup>a</sup> Mohamad Etesami,<sup>a</sup> Jayaraman Theerthagiri,<sup>b</sup> Myong Yong Choi,<sup>b</sup> Suttipong Wannapaiboon,<sup>c</sup> Mai Thanh Nguyen,<sup>d</sup> Tetsu Yonezawa<sup>d</sup> and Soorathep Kheawhom<sup>\*a,e,f</sup>

Due to their affordability and good catalytic activity for oxygen reactions, MOF-derived carbon composites containing metal alloys have piqued interest. However, during synthesis, MOFs have the disadvantage of causing significant carbon evaporation, resulting in a reduction of active sites and durability. This study proposes tailoring the molecular structure of MOFs by optimizing bipyridine and flexible 4-aminodiacetic terephthalic acid ligands, which have numerous coordination modes and framework structures, resulting in fascinating architectures. MOF frameworks having optimized N and O units are coordinated with Co and Ni ions to provide MOF precursors that are annealed at 700 °C in argon. The MOF-derived Co<sub>9</sub>S<sub>8</sub>/Co–N<sub>x</sub>/CoNi/Ni<sub>3</sub>S<sub>2</sub>@CNS-4 catalyst exhibits excellent catalytic activity, revealing an ORR half-wave potential of 0.86 V and an overpotential (OER) of 196 mV at 10 mA cm<sup>-2</sup>, a potential gap of 0.72 V and a Tafel slope of 79 mV dec<sup>-1</sup>. The proposed strategy allows for the rational design of N-coordinated Co and CoNi alloys attached to ultrathin N, S co-doped graphitic carbon sheets to enhance bifunctional activity and sufficient active sites. Consequently, the zinc–air battery using the synthesized catalyst shows a high peak power density of 206.9 mW cm<sup>-2</sup> (Pt/C + RuO<sub>2</sub> 116.1 mW cm<sup>-2</sup>), a small polarization voltage of 0.96 V after 370 h at 10 mA cm<sup>-2</sup>, and an outstanding durability of over 2400 cycles (400 h). The key contributions to the superior performance are the synergetic effects of the CoNi alloys plus the N,S-incorporated carbon skeleton, due to the small charge transfer resistances and enhanced active sites of CoNi, metal–S, and pyridinic N.

 Received 8th September 2022,  
 Accepted 6th November 2022

DOI: 10.1039/d2nr04933c

[rsc.li/nanoscale](http://rsc.li/nanoscale)

## 1. Introduction

In a wide range of energy conversion and storage technologies, the oxygen reduction reaction (ORR) and the oxygen evolution

reaction (OER) both play crucial roles in hydrogen electrolyzers, fuel cells, and rechargeable metal–air batteries.<sup>1–4</sup> However, enhancing the ORR and OER activities remains a significant problem due to complex mechanisms, intermediates, and huge energy barriers.<sup>5,6</sup> Noble metal catalysts *i.e.* ORR (Pt/C) and OER (RuO<sub>2</sub>/IrO<sub>2</sub>) are limited in their use for commercial applications due to high cost and lack of resources.<sup>7,8</sup> Furthermore, none of them have enough bifunctional activity for both the ORR and OER making them unsuitable for the bifunctional activities of rechargeable Zn–air batteries.<sup>9,10</sup> It is important for these electrochemical devices to develop multifunctional catalysts with highly efficient ORR and OER kinetics.<sup>11</sup> Recently, alternative non-noble metal based electrocatalysts (Fe, Co, Ni, Mn, and Mo),<sup>12,13</sup> metal alloys,<sup>14</sup> carbon-based materials,<sup>15–18</sup> transition metal oxides<sup>19,20</sup>/hydroxides<sup>21</sup>/MOFs<sup>22–24</sup> and their hybrids<sup>25</sup> have been extensively investigated as highly efficient and low-cost oxygen catalysts for bifunctional activities. As a result, finding a suitable material for non-noble metal electrocatalysts with remarkable stability,

<sup>a</sup>Department of Chemical Engineering, Faculty of Engineering, Chulalongkorn University, Bangkok 10330, Thailand. E-mail: soorathep.k@chula.ac.th

<sup>b</sup>Core-Facility Center for Photochemistry & Nanomaterials, Department of Chemistry (BK21 FOUR), Research Institute of Natural Sciences, Gyeongsang National University, Jinju 52828, Republic of Korea

<sup>c</sup>Synchrotron Light Research Institute, 111 University Avenue, Muang District, Nakhon Ratchasima 30000, Thailand

<sup>d</sup>Division of Materials Science and Engineering, Faculty of Engineering, Hokkaido University, Hokkaido 060-8628, Japan

<sup>e</sup>Bio-Circular-Green-economy Technology & Engineering Center (BCGeTEC), Faculty of Engineering, Chulalongkorn University, Bangkok 10330, Thailand

<sup>f</sup>Center of Excellence on Advanced Materials for Energy Storage, Chulalongkorn University, Bangkok 10330, Thailand

† Electronic supplementary information (ESI) available. See DOI: <https://doi.org/10.1039/d2nr04933c>



high specific surface areas, large pores, and lots of active sites is important.<sup>26</sup>

Metal–organic frameworks (MOFs) with excellent architecture and large surface areas capable of enabling reactions *via* electron transport in energy storage or conversion process are promising new platforms for electrocatalysis.<sup>27</sup> A combination of rich porosity and intrinsic nanopores (less than 100 nm diameter pores) provides a favorable environment for the development and preparation of exceptionally well-organized oxygen electrocatalysts.<sup>28,29</sup> MOFs also contain inorganic components such as layers, clusters, chains, or three-dimensional arrangements that are linked to organic linkers *via* strong bonds with complexing groups such as phosphonates, carboxylates, and N-containing chemicals.<sup>30,31</sup> Prior studies in the electrochemical field have focused on element doping and size modification of catalysts using MOF precursors.<sup>32</sup> Existing research suggested that changing the morphologies can change catalytic performance.<sup>33</sup> It is therefore still highly desirable but challenging to develop novel methods for the synthesis of morphology-controlled MOF templates to get customized active components and structures with high electrocatalytic performance.<sup>34,35</sup> In practice, controlling coordination geometry like oxidation state of metal cations, binding modes of ligands and solvent molecules is critical for the creation of MOFs with morphological and structural diversity.<sup>36</sup> Ligands can effectively adopt the topology of coordination nodes, various binding modes and certain solvent molecules to compete for unoccupied metal sites.<sup>37</sup> Due to the favorable rearrangement of electronic structures to minimize kinetic energy barriers, a multi-metallic species frequently generates synergistically improved catalytic activity.<sup>38</sup> Furthermore, during the calcination of MOFs, the inclusion of a secondary metal can inhibit the total agglomeration kinetics of each metal (MOFs).<sup>38</sup>

Lately, MOF-derived nonprecious bimetallic alloy materials, particularly using transition metals, have received much attention as oxygen electrocatalysts, because of their highly active catalytic activities in the ORR and OER. Several findings have shown that metal alloy catalysts such as FeCo,<sup>39,40</sup> FeNi,<sup>32,41</sup> Fe–Mn,<sup>42</sup> and NiCo<sup>14,15,43</sup> have better activity than their single metal materials and that the intrinsic polarity that can be provided by a connection between two metals might help catalytic activities. It is noted that metal alloys without a carbon support cannot achieve outstanding ORR/OER performance. The combination of metal alloy nanoparticles with hetero atoms and graphitic carbon that have high stability, superior conductivity. A large active surface area is preferable for enhancing the catalytic activity of alloy-based materials, thus favors increasing the number of active sites, as well as protecting metal alloy nanoparticles from aggregation. For example, Sheng *et al.* (2021) reported an efficient oxygen electrocatalyst made of NiCo alloy nanoparticles anchored on a carbon nanorod decorated with CNTs.<sup>44</sup> Tan *et al.* (2022) observed that the electronic structure of the encapsulated CoNi alloy exhibited good reversible oxygen catalytic activity and stability.<sup>45</sup> Thangasamy *et al.* (2022) investigated CoPi–NPC

nanosheets for the ORR in ZABs.<sup>46</sup> Furthermore, Sim *et al.* (2022) demonstrated that iron–cobalt/cobalt–nickel oxide dispersed on a reduced graphene oxide electrode exhibited superior stability at a high current density and high-rate rechargeable ZABs.<sup>12</sup>

During synthesis, MOFs have the drawback of carbon evaporation causing significantly reduced active sites and catalytic durability. However, this work suggests tailoring the molecular architectures of MOFs using the optimization of flexible multicarboxylate and 4,4-bpy ligands. The electrocatalysts were derived from bimetallic MOFs having different ratios of ligands *i.e.* 4,4-bipyridine (4,4-bpy) and 4-aminodiacetic terephthalic acid (H<sub>4</sub>adtp) in the presence of polar solvents. It is acknowledged that electrochemical activities (ORR and OER) and ZAB performance can be controlled by varying the ratios of 4,4-bpy and H<sub>4</sub>adtp ligands. The corresponding electrochemical performance of the heterostructure built of bimetallic sulfide and alloy composite materials was enhanced in terms of electron transport, adsorption optimization, and durability. The method is simple, rapid, and low-cost, and it sheds light on the synthesis of high-efficiency reversible oxygen electrocatalysts for large-scale production of a variety of energy devices such as electrolytes, fuel cells, and metal–air batteries.

## 2. Experimental section

### 2.1. Chemicals and materials

Commercially available materials such as nickel(II) sulfamate tetrahydrate, cobalt(II) acetate tetrahydrate, and 4,4-bipyridine, purchased from Merck, were used as received. For all experiments, analytical grade solvents: ethanol, dimethylformamide and deionized water were used. As described previously in the literature, 4-aminodiacetic terephthalic acid was synthesized (Scheme S1†).<sup>47</sup> CoNi alloy nanoparticles were prepared by the method reported previously.<sup>48</sup> Ni foam, 1 mm thick, was employed as a substrate for an air electrode and as a current collector for a negative electrode (Qijing Trading Co., Ltd). The Ni foam was cleaned with 37% hydrochloric acid (Qchemical Co., Ltd). Both zinc acetate (Merck) and potassium hydroxide pellets (CT Chemical Co., Ltd) were used to make the electrolyte. For the anode, a 2 mm thick Zn sheet (Zn 99.995 percent) was purchased from Sirikul Engineering Ltd.

### 2.2. Synthesis of bimetallic MOF precursors

An ethanolic solution of (10 ml) of 4,4-bipyridine (0.156 g, 2 mmol) was added dropwise to a stirred solution of Ni (SO<sub>3</sub>NH<sub>2</sub>)<sub>2</sub>·4H<sub>2</sub>O (0.325 g, 1 mmol) and Co(CH<sub>3</sub>COO)<sub>2</sub>·4H<sub>2</sub>O (0.249 g, 1 mmol), containing dimethylformamide (10 ml); H<sub>4</sub>adtp (0.253 g, 1 mmol) in water (10 ml) was added dropwise to the mixture. As a result, the solution color changed from green to light blue. The mixture was stirred continuously for 6 h at ambient temperature and pH was adjusted to 8 using concentrated HCl. After the solution was transferred to a 100 ml Teflon lined autoclave, it was kept in an oil bath for



72 h (120 °C). After cooling, the obtained blue precipitate of the MOF precursors was washed several times with distilled water and ethanol before being dried in a vacuum oven (60 °C for 6 h).

### 2.3. Synthesis of electrocatalysts

The resulting precursors were pyrolyzed in a tube furnace at 700 °C for 2 hours in an argon environment at a heating rate of 3 °C min<sup>-1</sup>. Following that, a dandelion flower-like hierarchical catalyst made of N and S co-doped carbon and carbon-encapsulated CoNi alloy nanoparticles was prepared. The catalysts *viz.* Co<sub>9</sub>S<sub>8</sub>/CoNi/Ni<sub>3</sub>S<sub>2</sub>@CNS-1, Co<sub>9</sub>S<sub>8</sub>/Co-N<sub>x</sub>/CoNi/Ni<sub>3</sub>S<sub>2</sub>@CNS-2, Co<sub>9</sub>S<sub>8</sub>/CoNi/Ni<sub>3</sub>S<sub>2</sub>@CNS-3, and Co<sub>9</sub>S<sub>8</sub>/Co-N<sub>x</sub>/CoNi/Ni<sub>3</sub>S<sub>2</sub>@CNS-4 were obtained by optimizing the ligand

ratios. Supporting documentation contains details about electrocatalyst characterization, electrochemical measurement, electrode fabrication of the air cathode and assembly of ZABs.

## 3. Results and discussion

### 3.1. Synthesis

The hierarchical electrocatalyst was prepared using a reaction of 4,4-bpy and 4-aminodiacetic terephthalic acid ligands and Ni and Co metal ions in the presence of DMF/ethanol/water. The use of neutral N-donor ligands (4,4-bpy), as pillars to space 2D layers based on polycarboxylate ligands, is an effective and controllable method of generating hierarchical architectures.<sup>49</sup> Architectures are frequently built with mixed ligands as linkers; single linkers are uncommon because most linkers are difficult to build in one mode while spacing them in the other. Fig. 1 shows the distinct function of both linkers *viz.* 4,4-bipyridine and 4-aminodiacetic terephthalic acid. Compared with aromatic rigid carboxylates (BTC),<sup>50</sup> the flexible multidentate iminodiacetate functionality can easily chelate and bridge metals by adopting diverse bonding modes. Nickel-cobalt MOF clusters were generated homogeneously and remodeled into carbon frameworks after drying and subsequent carbonization at 700 °C for 2 h under an Ar atmosphere. The ligands in the MOF structures (4,4-bpy and H<sub>4</sub>adtp) can be easily optimized with a constant molar ratio of 1 : 1 for Ni<sup>2+</sup> and Co<sup>2+</sup>, as shown in Fig. 2. Controlled calcination can produce CoNi alloy nanoparticle/carbon composites derived from MOFs with unique structures, tailorable porosity, and large surface areas suitable for electrocatalytic applications (OER/ORR).<sup>51</sup> During the heat treatment process, the formation of alloy nanoparticles and carbon materials occurs simultaneously, and the CoNi-based nanoparticles may be uniformly dispersed in carbon frameworks, which is still extre-

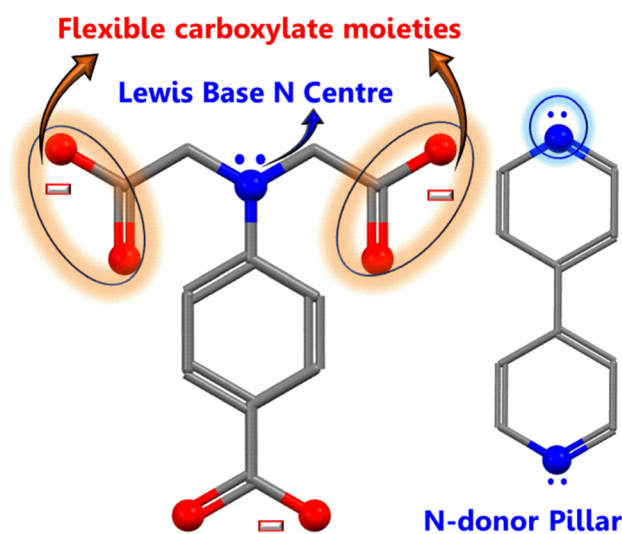


Fig. 1 Ligand structures demonstrating their distinct functionalities.



Electrocatalysts	4,4-Bpy (mmol)	H <sub>3</sub> adtp (mmol)
Co <sub>9</sub> S <sub>8</sub> /CoNi/Ni <sub>3</sub> S <sub>2</sub> @CNS-1	-	2
Co <sub>9</sub> S <sub>8</sub> /Co-N <sub>x</sub> /CoNi/Ni <sub>3</sub> S <sub>2</sub> @CNS-2	1	1
Co <sub>9</sub> S <sub>8</sub> /CoNi/Ni <sub>3</sub> S <sub>2</sub> @CNS-3	1	3
Co <sub>9</sub> S <sub>8</sub> /Co-N <sub>x</sub> /CoNi/Ni <sub>3</sub> S <sub>2</sub> @CNS-4	3	1

Fig. 2 Scheme for the synthesis of electrocatalysts 1–4 (CoS/CoN/CoNi/Co–N@CNS) optimizing the ligand concentration.



mely difficult to achieve *via* other methods. Furthermore, carbonaceous materials used in three-dimensional porous hierarchical designs have been proven as an effective way to enhance electrocatalytic performance.<sup>52,53</sup> Thus, a variety of interconnected nanostructures are created when metal-based nanoparticles are incorporated into three-dimensional carbon frameworks with voids.<sup>38</sup> The entire synthetic process is quite simple and facile, requiring only an oil bath and subsequently a tubular furnace.

### 3.2. Morphological and structural analysis

Images from field-emission scanning electron microscopy (FE-SEM) reveal polyhedral structures with multilayered structures. In Fig. 3a, the prepared MOFs display homogeneous spherical surfaces, indicating that multi-carboxylate and 4,4-bpy were uniformly coordinated on the Ni-Co ion center. In Fig. 3b, after pyrolysis, dandelion flower-like structures (3  $\mu\text{m}$ ) with a rough surface are observed; their edges still had a

similar spheroid morphology. The Ni-Co elements are largely found in the particles and overlap with the N and S elements, indicating the formation of CoNi alloy nanoparticles. Consequently, the diameters of the carbon nanofibers are seen to differ due to the optimization of the ligands (50–100 nm). In Fig. 3c–f, the catalyst morphology was investigated further using TEM and EDS. The hierarchical structure of  $\text{Co}_9\text{S}_8/\text{Co-N}_x/\text{CoNi}/\text{Ni}_3\text{S}_2@\text{CNS-4}$  with extended graphitic carbon networks on the surface of carbon polyhedra is confirmed *via* TEM. In Fig. 3c, CoNi alloys show a polyhedron-like shape with less than 10 nm diameter nanoparticles hanging on the surface and edges. In Fig. 3d and S2,<sup>†</sup> the metal sulfides ( $\text{Co}_9\text{S}_8$  and  $\text{Ni}_3\text{S}_2$ ) appear homogeneous on the surface carbon structures.<sup>54</sup> The creation of the heterojunction<sup>55</sup> is further confirmed by high-resolution TEM (HRTEM), which also exhibits distinct lattice fringes and close contact between  $\text{Co}_9\text{S}_8$  (440) and  $\text{Ni}_3\text{S}_2$  (110) as shown in Fig. 3d and e. In Fig. 3f (inset), the (111) plane of CoNi and the (002) plane of carbon

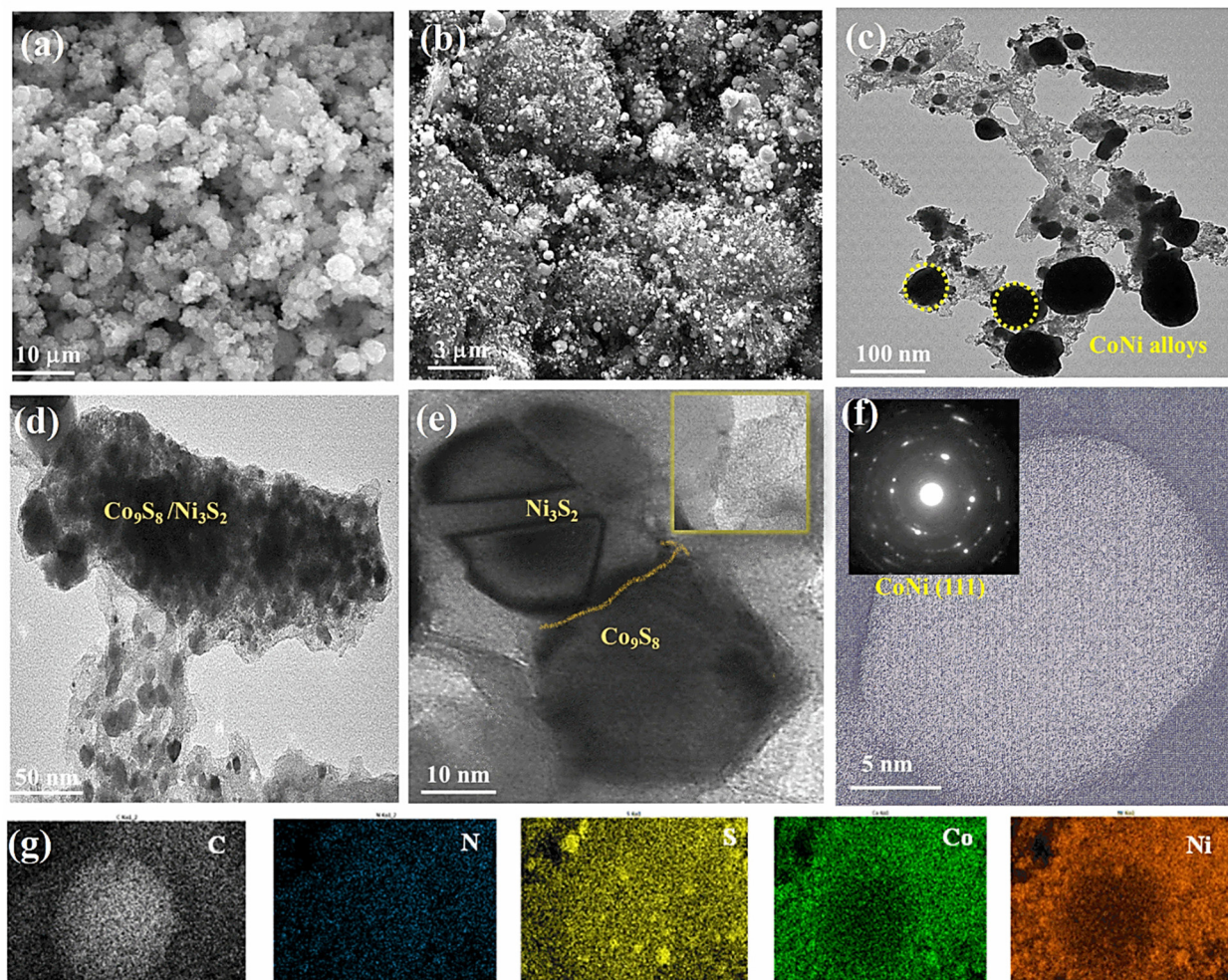


**Fig. 3** (a) FE-SEM images of MOF precursor-4 and that (b) after calcination of the corresponding dandelion flowers like  $\text{Co}_9\text{S}_8/\text{Co-N}_x/\text{CoNi}/\text{Ni}_3\text{S}_2@\text{CNS-4}$  catalyst, (c–e) TEM images of  $\text{Co}_9\text{S}_8/\text{Co-N}_x/\text{CoNi}/\text{Ni}_3\text{S}_2@\text{CNS-4}$ ,  $\text{Co}_9\text{S}_8/\text{Ni}_3\text{S}_2$  and their heterojunction, (f) TEM image of CoNi alloy nanoparticle; inset show derived fast Fourier transform SAED patterns, and (g) EDS mappings for carbon (C), nitrogen (N), sulphur (S), cobalt (Co) and nickel (Ni).













**Fig. 6** Electrocatalytic ORR performances: (a) LSV curves of CoS/Co-N<sub>x</sub>/CoNi/NiS<sub>2</sub>@CNS 1–4, commercial 20% Pt/C and Pt/C + RuO<sub>2</sub> in O<sub>2</sub>-saturated 0.1 M KOH, (b) LSV curves of CoS/Co-N<sub>x</sub>/CoNi/NiS<sub>2</sub>@CNS-4, at various rotation rates, (c) Tafel plots of catalysts 1–4 and Pt/C, (d) Electron transfer number (*n*) of catalysts 1–4, and Pt/C, inset: the corresponding peroxide yields, (e) EIS spectra of catalysts 1–4, and (f) chronoamperometric responses of Co<sub>9</sub>S<sub>8</sub>/Co-N<sub>x</sub>/CoNi/Ni<sub>3</sub>S<sub>2</sub>@CNS-4, and commercial 20% Pt/C in O<sub>2</sub>-saturated 0.1 M KOH solution at a rotation rate of 1600 rpm at ~0.4 V vs. RHE.

lyst Co<sub>9</sub>S<sub>8</sub>/Co-N<sub>x</sub>/CoNi/Ni<sub>3</sub>S<sub>2</sub>@CNS-4 exhibits the lowest charge transfer resistance, among the three catalysts 1–3, having a noticeably smaller semicircle in the intermediate frequency region (Table S2<sup>†</sup>). As shown in Fig. 6f, the long-term durability of Co<sub>9</sub>S<sub>8</sub>/Co-N<sub>x</sub>/CoNi/Ni<sub>3</sub>S<sub>2</sub>@CNS-4 and commercial Pt/C electrocatalyst was investigated using chronoamperometric experiments. Only 16% catalytic activity loss was discovered on the surface of the Co<sub>9</sub>S<sub>8</sub>/Co-N<sub>x</sub>/CoNi/Ni<sub>3</sub>S<sub>2</sub>@CNS-4 electrode after more than 24 h of continuous chronoamperometric analysis, demonstrating the superior stability of catalyst 4 to the commercial Pt/C electrocatalyst. This outcome was brought about by the stronger incorporation of metal sulfides, nitrogen-coordinated Co, and CoNi alloys into the porous graphitic carbon framework, which increased the electrochemical ORR activity and endurance. In Fig. 6f (inset), the catalyst was tested against methanol poisoning to prove its applicability in direct methanol fuel cells (DMFCs). The catalyst Co<sub>9</sub>S<sub>8</sub>/Co-N<sub>x</sub>/CoNi/Ni<sub>3</sub>S<sub>2</sub>@CNS-4 showed strong resistance to methanol because there was no current density loss when 2.0 mL of methanol (CH<sub>3</sub>OH) was added to the 0.1 M KOH solution. On the other hand, the commercial Pt/C electrocatalyst exhibit a considerable decrease in cathodic current density during the addition of CH<sub>3</sub>OH because of the methanol oxidation process being facilitated on the Pt/C catalytically active surface sites. These findings indicate that Co<sub>9</sub>S<sub>8</sub>/Co-N<sub>x</sub>/CoNi/Ni<sub>3</sub>S<sub>2</sub>@CNS-4 can be exploited as a possible cathodic material in the exciting

field of ZABs since catalyst 4 has excellent ORR kinetics, outstanding durability, and strong resistance to methanol poisoning. It is noted that the unique hierarchical porous structure and interfacial synergy between the CoNi, CoN, Ni<sub>3</sub>S<sub>2</sub>, and Co<sub>9</sub>S<sub>8</sub> nanoparticle structures with rich defects can increase mass transfer and graphitization to a degree that is advantageous for electron transport.

### 3.4. Oxygen evolution reaction (OER)

As shown in Fig. 7a, OER performance of the electrocatalysts and the commercial RuO<sub>2</sub>/PtC + RuO<sub>2</sub> catalysts were evaluated. Results were compared with the well-developed transition metal alloy catalysts reported recently (Table S1<sup>†</sup>). It is seen that Co<sub>9</sub>S<sub>8</sub>/Co-N<sub>x</sub>/CoNi/Ni<sub>3</sub>S<sub>2</sub>@CNS-4 (1.58 V) and Co<sub>9</sub>S<sub>8</sub>/Co-N<sub>x</sub>/CoNi/Ni<sub>3</sub>S<sub>2</sub>@CNS-2 (1.61 V) both possessed low overpotentials of 196 and 201 mV at 10 mA cm<sup>-2</sup>, which are smaller than the commercial RuO<sub>2</sub> (203 mV) and associated with the synergy between Co<sub>9</sub>S<sub>8</sub> and Ni<sub>3</sub>S<sub>2</sub> in catalyst-4. In contrast, Co<sub>9</sub>S<sub>8</sub>/CoNi/Ni<sub>3</sub>S<sub>2</sub>@CNS-1 (205 mV) and Co<sub>9</sub>S<sub>8</sub>/Co-N<sub>x</sub>/CoNi/Ni<sub>3</sub>S<sub>2</sub>@CNS-3 (211 mV) catalysts have high overpotential of catalysts. However, the OER performance of prepared catalysts 1–4 proved to be superior to the recently reported catalysts (Table S1<sup>†</sup>). The results indicated that bimetallic alloys and sulfides acted positively in promoting the performance of the OER.<sup>54</sup> As shown in Fig. 7b, the Co<sub>9</sub>S<sub>8</sub>/Co-N<sub>x</sub>/CoNi/Ni<sub>3</sub>S<sub>2</sub>@CNS-4 catalyst had the smallest Tafel value (79.51 mV





Fig. 7 Electrocatalytic OER performances: (a) LSV curves of CoS/Co-N<sub>x</sub>/CoNi/Ni<sub>3</sub>S<sub>2</sub>@CNS 1–4, commercial RuO<sub>2</sub> and Pt/C + RuO<sub>2</sub> in N<sub>2</sub>-saturated 0.1 M KOH, (b) Tafel plots of LSV curves of catalysts 1–4, RuO<sub>2</sub> and Pt/C + RuO<sub>2</sub>, (c) EIS spectra of catalysts 1–4, and (d) chronoamperometric responses of Co<sub>9</sub>S<sub>8</sub>/Co-N/CoNi/Ni<sub>3</sub>S<sub>2</sub>@CNS-4, and commercial RuO<sub>2</sub> in N<sub>2</sub>-saturated 0.1 M KOH solution.

dec<sup>-1</sup>) among all as-prepared catalysts: Co<sub>9</sub>S<sub>8</sub>/CoNi/Ni<sub>3</sub>S<sub>2</sub>@CNS-1 (130.74 mV dec<sup>-1</sup>), Co<sub>9</sub>S<sub>8</sub>/Co-N<sub>x</sub>/CoNi/Ni<sub>3</sub>S<sub>2</sub>@CNS-2 (119.38 mV dec<sup>-1</sup>) and Co<sub>9</sub>S<sub>8</sub>/CoNi/Ni<sub>3</sub>S<sub>2</sub>@CNS-3 (91 mV dec<sup>-1</sup>); all indicating fast OER kinetics. As shown in Fig. 7c, the EIS measurements based on the Nyquist plot revealed that of the three samples, Co<sub>9</sub>S<sub>8</sub>/Co-N<sub>x</sub>/CoNi/Ni<sub>3</sub>S<sub>2</sub>@CNS-4 had the shortest semicircle. The potential gap  $\Delta E$  between the ORR and OER ( $E = E_{j10} - E_{1/2}$ ) has been used to evaluate an electrocatalyst's total bifunctional activity. Consequently, Co<sub>9</sub>S<sub>8</sub>/Co-N<sub>x</sub>/CoNi/Ni<sub>3</sub>S<sub>2</sub>@CNS-4 had a tiny  $\Delta E$  value of 0.72 V, which is comparable to the most recently described metal-involving oxygen electrocatalysts (Fig. S10d†).<sup>12,18</sup> In contrast to benchmark Pt/C and RuO<sub>2</sub>, which decreased after the 24 h tests, the performance of catalyst 4 did not significantly decline after continuous operation for 24 hours at 10 mA cm<sup>-2</sup> according to the long-term durability test, representing that the material had good bifunctional catalytic stability, as shown in Fig. 7d. The superior ORR and OER activities of the Co<sub>9</sub>S<sub>8</sub>/Co-N<sub>x</sub>/CoNi/Ni<sub>3</sub>S<sub>2</sub>@CNS-4 catalyst can be attributed to the following factors based on the above results: firstly, the optimized ligand concentration in

catalyst-4 had a high surface area, hierarchical pores, and defect rich structures, which helped to increase the number of electroactive sites, enhancing reactions and electrocatalytic performance. Secondly, the 2D graphitic carbon polyhedron heterogeneous structure with N and S elements was able to boost catalytic processes at the interface and provide long-range conductivity. Finally, the porous multi-compound system of the Co<sub>9</sub>S<sub>8</sub>, Co-N<sub>x</sub>, CoNi alloy nanoparticles, and Ni<sub>3</sub>S<sub>2</sub> enhanced the electrochemical kinetics by synergistically facilitating charge/ion diffusion and increasing the interfacial contact between the electrolyte and the electrode. A comparison of ORR/OER catalytic activity with that of a previously published transition metal and heteroatom-doped carbon composite catalyst, as shown in Table S1,† further supports the exceptional bifunctional activity of Co<sub>9</sub>S<sub>8</sub>/Co-N<sub>x</sub>/CoNi/Ni<sub>3</sub>S<sub>2</sub>@CNS-4 in our work.

### 3.5. Zinc-air battery performance

The Co<sub>9</sub>S<sub>8</sub>/Co-N<sub>x</sub>/Co-Ni/Ni<sub>3</sub>S<sub>2</sub>@CNS-4 catalyst utilized in real ZABs (Fig. 8a) as an air cathode was properly evaluated based on its better ORR/OER activities. Thus, an aqueous recharge-





**Fig. 8** Zn-air battery (ZABs) performances: (a) schematic representation of the assembled rechargeable ZABs (b) open-circuit voltage curves of ZABs using  $\text{Co}_9\text{S}_8/\text{Co-N}_x/\text{CoNi/Ni}_3\text{S}_2@\text{CNS-4}$  and  $\text{Pt/C} + \text{RuO}_2$  air cathodes, (c) and (d) charge and discharge polarization curves and the corresponding power density curves, (e) specific capacity plots at  $10 \text{ mA cm}^{-2}$ , (f) discharge curves at different current densities of  $\text{Co}_9\text{S}_8/\text{Co-N}_x/\text{CoNi/Ni}_3\text{S}_2@\text{CNS-4}$  and  $\text{Pt/C} + \text{RuO}_2$ ; (g) galvanostatic cycling stability tests of the zinc-air battery with  $\text{Co}_9\text{S}_8/\text{Co-N}_x/\text{CoNi/Ni}_3\text{S}_2@\text{CNS-4}$  and  $\text{Pt/C} + \text{RuO}_2$  and (h) the photos of two ZABs connected in series to drive green LED lights.

able Zn-air battery was prepared using catalyst  $\text{Co}_9\text{S}_8/\text{Co-N}_x/\text{CoNi/Ni}_3\text{S}_2@\text{CNS-4}$  as the air cathode. Comparisons were made between its performance and that of the catalyst used in commercial air cathodes ( $\text{Pt/C} + \text{RuO}_2$ , mixed catalyst, 1:1 ratio). It was found that the ZAB based on  $\text{Co}_9\text{S}_8/\text{Co-N}_x/\text{CoNi/Ni}_3\text{S}_2@\text{CNS-4}$  had an open circuit potential (OCP) of 1.59 V (Fig. 8b), which is greater than that of the  $\text{Pt/C} + \text{RuO}_2$  catalyst (1.47 V) and recently published bifunctional catalysts (Table S3<sup>†</sup>). In Fig. 8c, both discharge and charge polarization curves of  $\text{Co}_9\text{S}_8/\text{Co-N}_x/\text{CoNi/Ni}_3\text{S}_2@\text{CNS-4}$  are observed to display a smaller voltage gap than  $\text{Pt/C} + \text{RuO}_2$  due to its strong bifunctional activities. In Fig. 8d, catalyst 4 based ZABs exhibited a peak power density of  $206.9 \text{ mA cm}^{-2}$  at  $325 \text{ mA cm}^{-2}$ , outperforming  $\text{Pt/C} + \text{RuO}_2$  ( $116.1 \text{ mW cm}^{-2}$ ). The presence of micro- and mesopore structures in the  $\text{Co}_9\text{S}_8/\text{Co-N}_x/\text{CoNi/Ni}_3\text{S}_2@\text{CNS-4}$  was found to be primarily responsible for

the high electrochemically active surface areas, which facilitated the transport of mass electrons during performance. A specific capacity of  $801 \text{ mA h g}^{-1}$  for the collectively exhaustive  $\text{Co}_9\text{S}_8/\text{Co-N}_x/\text{CoNi/Ni}_3\text{S}_2@\text{CNS-4}$  was obtained from the galvanostatic discharge curve at a current density of  $10 \text{ mA cm}^{-2}$ , as shown in Fig. 8e. This was somewhat higher than the ZAB using the  $\text{Pt/C} + \text{RuO}_2$  ( $762 \text{ mA h g}^{-1}$ ) air cathode. Furthermore, under different discharge current densities,  $\text{Co}_9\text{S}_8/\text{Co-N}_x/\text{CoNi/Ni}_3\text{S}_2@\text{CNS-4}$  demonstrated a significant rate capability (Fig. 8f). In Fig. 8g, long-term cyclability testing at  $10 \text{ mA cm}^{-2}$  revealed that  $\text{Co}_9\text{S}_8/\text{Co-N}_x/\text{CoNi/Ni}_3\text{S}_2@\text{CNS-4}$  had a narrow initial voltage gap of 0.96 V and no significant voltage attenuation after cycling for more than 370 h (Fig. S11<sup>†</sup>), which was significantly better than the cycle time of  $\text{Pt/C} + \text{RuO}_2$ -based ZABs (only 50 h). In Fig. 8h, two catalyst-4-based ZABs are connected in series facilitating green light-





- 12 W. J. Sim, M. T. Nguyen, Z. Huang, S. Kheawhom, C. Wattanakit and T. Yonezawa, *Nanoscale*, 2022, **14**, 8012–8022, DOI: [10.1039/D2NR01258H](https://doi.org/10.1039/D2NR01258H).
- 13 M. D. Bhatt and J. Y. Lee, *Energy Fuels*, 2020, **34**, 6634–6695, DOI: [10.1021/acs.energyfuels.0c00953](https://doi.org/10.1021/acs.energyfuels.0c00953).
- 14 Y. Fu, H.-Y. Yu, C. Jiang, T.-H. Zhang, R. Zhan, X. Li, J.-F. Li, J.-H. Tian and R. Yang, *Adv. Funct. Mater.*, 2018, **28**, 1705094, DOI: [10.1002/adfm.201705094](https://doi.org/10.1002/adfm.201705094).
- 15 Z. Cai, I. Yamada and S. Yagi, *ACS Appl. Mater. Interfaces*, 2020, **12**, 5847–5856, DOI: [10.1021/acsami.9b19268](https://doi.org/10.1021/acsami.9b19268).
- 16 W. Wan, X. Liu, H. Li, X. Peng, D. Xi and J. Luo, *Appl. Catal., B*, 2019, **240**, 193–200, DOI: [10.1016/j.apcatb.2018.08.081](https://doi.org/10.1016/j.apcatb.2018.08.081).
- 17 J.-C. Li, P.-X. Hou, S.-Y. Zhao, C. Liu, D.-M. Tang, M. Cheng, F. Zhang and H.-M. Cheng, *Energy Environ. Sci.*, 2016, **9**, 3079–3084, DOI: [10.1039/C6EE02169G](https://doi.org/10.1039/C6EE02169G).
- 18 Z. Huang, M. T. Nguyen, W. J. Sim, M. Takahashi, S. Kheawhom and T. Yonezawa, *Sustainable Energy Fuels*, 2022, **6**, 3931–3943, DOI: [10.1039/D2SE00606E](https://doi.org/10.1039/D2SE00606E).
- 19 Y. Wang, R. Gan, Z. Ai, H. Liu, C. Wei, Y. Song, M. Dirican, X. Zhang, C. Ma and J. Shi, *Carbon*, 2021, **181**, 87–98, DOI: [10.1016/j.carbon.2021.05.016](https://doi.org/10.1016/j.carbon.2021.05.016).
- 20 Z. Bai, J. Heng, Q. Zhang, L. Yang and F. Chang, *Adv. Energy Mater.*, 2018, **8**, 1802390, DOI: [10.1002/aenm.201802390](https://doi.org/10.1002/aenm.201802390).
- 21 H. Yi, S. Liu, C. Lai, G. Zeng, M. Li, X. Liu, B. Li, X. Huo, L. Qin, L. Li, M. Zhang, Y. Fu, Z. An and L. Chen, *Adv. Energy Mater.*, 2021, **11**, 2002863, DOI: [10.1002/aenm.202002863](https://doi.org/10.1002/aenm.202002863).
- 22 B. Y. Xia, Y. Yan, N. Li, H. B. Wu, X. W. Lou and X. Wang, *Nat. Energy*, 2016, **1**, 15006, DOI: [10.1038/nenergy.2015.6](https://doi.org/10.1038/nenergy.2015.6).
- 23 H.-F. Wang, L. Chen, H. Pang, S. Kaskel and Q. Xu, *Chem. Soc. Rev.*, 2020, **49**, 1414–1448, DOI: [10.1039/C9CS00906J](https://doi.org/10.1039/C9CS00906J).
- 24 Z. Li, R. Gao, M. Feng, Y.-P. Deng, D. Xiao, Y. Zheng, Z. Zhao, D. Luo, Y. Liu, Z. Zhang, D. Wang, Q. Li, H. Li, X. Wang and Z. Chen, *Adv. Energy Mater.*, 2021, **11**, 2003291, DOI: [10.1002/aenm.202003291](https://doi.org/10.1002/aenm.202003291).
- 25 L. Zou, Y.-S. Wei, C.-C. Hou, C. Li and Q. Xu, *Small*, 2021, **17**, 2004809, DOI: [10.1002/smll.202004809](https://doi.org/10.1002/smll.202004809).
- 26 Z. Liang, T. Qiu, S. Gao, R. Zhong and R. Zou, *Adv. Energy Mater.*, 2022, **12**, 2003410, DOI: [10.1002/aenm.202003410](https://doi.org/10.1002/aenm.202003410).
- 27 C.-C. Hou and Q. Xu, *Adv. Energy Mater.*, 2019, **9**, 1801307, DOI: [10.1002/aenm.201801307](https://doi.org/10.1002/aenm.201801307).
- 28 C. Li, S. Dong, P. Wang, C. Wang and L. Yin, *Adv. Energy Mater.*, 2019, **9**, 1902352, DOI: [10.1002/aenm.201902352](https://doi.org/10.1002/aenm.201902352).
- 29 G. Li, S. Zhao, Y. Zhang and Z. Tang, *Adv. Mater.*, 2018, **30**, 1800702, DOI: [10.1002/adma.201800702](https://doi.org/10.1002/adma.201800702).
- 30 W.-H. Li, W.-H. Deng, G.-E. Wang and G. Xu, *EnergyChem*, 2020, **2**, 100029, DOI: [10.1016/j.enchem.2020.100029](https://doi.org/10.1016/j.enchem.2020.100029).
- 31 H. Wu, M. Almalki, X. Xu, Y. Lei, F. Ming, A. Mallick, V. Roddatis, S. Lopatin, O. Shekhah, M. Eddaoudi and H. N. Alshareef, *J. Am. Chem. Soc.*, 2019, **141**, 20037–20042, DOI: [10.1021/jacs.9b11446](https://doi.org/10.1021/jacs.9b11446).
- 32 D. Xie, D. Yu, Y. Hao, S. Han, G. Li, X. Wu, F. Hu, L. Li, H.-Y. Chen, Y.-F. Liao and S. Peng, *Small*, 2021, **17**, 2007239, DOI: [10.1002/smll.202007239](https://doi.org/10.1002/smll.202007239).
- 33 S. N. Khan, S. Ge, Y. Huang, H. Xu, W. Yang, R. Hong, Y. Mai, E. Gu, X. Lin and G. Yang, *Sci. China Mater.*, 2022, **65**, 612–619, DOI: [10.1007/s40843-021-1769-7](https://doi.org/10.1007/s40843-021-1769-7).
- 34 T. Guo, L. Chen, Y. Li and K. Shen, *Small*, 2022, **18**, 2107739, DOI: [10.1002/smll.202107739](https://doi.org/10.1002/smll.202107739).
- 35 Y. Xin, F. Wang, L. Chen, Y. Li and K. Shen, *Green Chem.*, 2022, **24**, 6544–6555, DOI: [10.1039/D2GC02426H](https://doi.org/10.1039/D2GC02426H).
- 36 Z. Zhang and M. J. Zaworotko, *Chem. Soc. Rev.*, 2014, **43**, 5444–5455, DOI: [10.1039/C4CS00075G](https://doi.org/10.1039/C4CS00075G).
- 37 B. Zheng, X. Sun, G. Li, A. J. Cairns, V. C. Kravtsov, Q. Huo, Y. Liu and M. Eddaoudi, *Cryst. Growth Des.*, 2016, **16**, 5554–5562, DOI: [10.1021/acs.cgd.6b01031](https://doi.org/10.1021/acs.cgd.6b01031).
- 38 M. K. Lee, M. Shokouhimehr, S. Y. Kim and H. W. Jang, *Adv. Energy Mater.*, 2022, **12**, 2003990, DOI: [10.1002/aenm.202003990](https://doi.org/10.1002/aenm.202003990).
- 39 C.-Y. Su, H. Cheng, W. Li, Z.-Q. Liu, N. Li, Z. Hou, F.-Q. Bai, H.-X. Zhang and T.-Y. Ma, *Adv. Energy Mater.*, 2017, **7**, 1602420, DOI: [10.1002/aenm.201602420](https://doi.org/10.1002/aenm.201602420).
- 40 Y. Xiong, Y. Yang, F. J. DiSalvo and H. D. Abruña, *J. Am. Chem. Soc.*, 2019, **141**, 10744–10750, DOI: [10.1021/jacs.9b03561](https://doi.org/10.1021/jacs.9b03561).
- 41 X. Xie, L. Shang, R. Shi, G. I. N. Waterhouse, J. Zhao and T. Zhang, *Nanoscale*, 2020, **12**, 13129–13136, DOI: [10.1039/D0NR02486D](https://doi.org/10.1039/D0NR02486D).
- 42 Z. Dong, G. Liu, S. Zhou, Y. Zhang, W. Zhang, A. Fan, X. Zhang and X. Dai, *ChemCatChem*, 2018, **10**, 5475–5486, DOI: [10.1002/cctc.201801412](https://doi.org/10.1002/cctc.201801412).
- 43 X. Xu, F. Ran, Z. Fan, Z. Cheng, T. Lv, L. Shao and Y. Liu, *ACS Appl. Mater. Interfaces*, 2020, **12**, 17870–17880, DOI: [10.1021/acsami.0c01572](https://doi.org/10.1021/acsami.0c01572).
- 44 K. Sheng, Q. Yi, A. L. Chen, Y. Wang, Y. Yan, H. Nie and X. Zhou, *ACS Appl. Mater. Interfaces*, 2021, **13**, 45394–45405, DOI: [10.1021/acsami.1c10671](https://doi.org/10.1021/acsami.1c10671).
- 45 Y. Tan, Z. Zhang, Z. Lei, L. Yu, W. Wu, Z. Wang and N. Cheng, *Appl. Catal., B*, 2022, **304**, 121006, DOI: [10.1016/j.apcatb.2021.121006](https://doi.org/10.1016/j.apcatb.2021.121006).
- 46 P. Thangasamy, S. Oh, H. Randriamahazaka, S. Nam and I.-K. Oh, *Appl. Catal., B*, 2022, **316**, 121656, DOI: [10.1016/j.apcatb.2022.121656](https://doi.org/10.1016/j.apcatb.2022.121656).
- 47 R. Maity, D. Chakraborty, S. Nandi, A. K. Yadav, D. Mullangi, C. P. Vinod and R. Vaidhyanathan, *ACS Appl. Nano Mater.*, 2019, **2**, 5169–5178, DOI: [10.1021/acsanm.9b01047](https://doi.org/10.1021/acsanm.9b01047).
- 48 W. Lu, D. Sun and H. Yu, *J. Alloys Compd.*, 2013, **546**, 229–233, DOI: [10.1016/j.jallcom.2012.08.063](https://doi.org/10.1016/j.jallcom.2012.08.063).
- 49 X. Meng, X.-Z. Song, S.-Y. Song, G.-C. Yang, M. Zhu, Z.-M. Hao, S.-N. Zhao and H.-J. Zhang, *Chem. Commun.*, 2013, **49**, 8483–8485, DOI: [10.1039/C3CC44106G](https://doi.org/10.1039/C3CC44106G).
- 50 M. F. Sanad, A. R. Puente Santiago, S. A. Tolba, M. A. Ahsan, O. Fernandez-Delgado, M. Shawky Adly, E. M. Hashem, M. Mahrous Abodouh, M. S. El-Shall, S. T. Sreenivasan, N. K. Allam and L. Echegoyen, *J. Am. Chem. Soc.*, 2021, **143**, 4064–4073, DOI: [10.1021/jacs.1c01096](https://doi.org/10.1021/jacs.1c01096).
- 51 J. Ren, Y. Huang, H. Zhu, B. Zhang, H. Zhu, S. Shen, G. Tan, F. Wu, H. He, S. Lan, X. Xia and Q. Liu, *Carbon Energy*, 2020, **2**, 176–202, DOI: [10.1002/cey2.44](https://doi.org/10.1002/cey2.44).



- 52 X. Chu, F. Meng, T. Deng and W. Zhang, *Nanoscale*, 2021, **13**, 5570–5593, DOI: [10.1039/D1NR00160D](https://doi.org/10.1039/D1NR00160D).
- 53 X. Wang, L. Li, M. Shi, Y. Wang, G. Xu, K. Yuan, P. Zhu, M. Ding and Y. Chen, *Chem. Sci.*, 2022, **13**, 11639–11647, DOI: [10.1039/D2SC03585E](https://doi.org/10.1039/D2SC03585E).
- 54 X. Wang, Y. Yang, R. Wang, L. Li, X. Zhao and W. Zhang, *Langmuir*, 2022, **38**, 7280–7289, DOI: [10.1021/acs.langmuir.2c00805](https://doi.org/10.1021/acs.langmuir.2c00805).
- 55 H. Chang, L.-N. Shi, Y.-H. Chen, P.-F. Wang and T.-F. Yi, *Coord. Chem. Rev.*, 2022, **473**, 214839, DOI: [10.1016/j.ccr.2022.214839](https://doi.org/10.1016/j.ccr.2022.214839).
- 56 Y. Shi, Z. Lyu, M. Zhao, R. Chen, Q. N. Nguyen and Y. Xia, *Chem. Rev.*, 2021, **121**, 649–735, DOI: [10.1021/acs.chemrev.0c00454](https://doi.org/10.1021/acs.chemrev.0c00454).
- 57 S. Li, E. Li, X. An, X. Hao, Z. Jiang and G. Guan, *Nanoscale*, 2021, **13**, 12788–12817, DOI: [10.1039/D1NR02592A](https://doi.org/10.1039/D1NR02592A).
- 58 F. Zeng, C. Mebrahtu, L. Liao, A. K. Beine and R. Palkovits, *J. Energy Chem.*, 2022, **69**, 301–329, DOI: [10.1016/j.jechem.2022.01.025](https://doi.org/10.1016/j.jechem.2022.01.025).
- 59 S. Kurungot, A. Pandikassala, G. Singla, T. S. Khan, M. A. Haider, V. Prabhakaran and V. Kashyap, *Nanoscale*, 2022, **14**, 15928–15941, DOI: [10.1039/D2NR04170G](https://doi.org/10.1039/D2NR04170G).
- 60 Z. Zhu, Q. Xu, Z. Ni, K. Luo, Y. Liu and D. Yuan, *ACS Sustainable Chem. Eng.*, 2021, **9**, 13491–13500, DOI: [10.1021/acssuschemeng.1c04259](https://doi.org/10.1021/acssuschemeng.1c04259).
- 61 K. Ghosh, M. Kumar, T. Maruyama and Y. Ando, *Carbon*, 2009, **47**, 1565–1575, DOI: [10.1016/j.carbon.2009.02.007](https://doi.org/10.1016/j.carbon.2009.02.007).
- 62 J. Qin, Z. Liu, D. Wu and J. Yang, *Appl. Catal., B*, 2020, **278**, 119300, DOI: [10.1016/j.apcatb.2020.119300](https://doi.org/10.1016/j.apcatb.2020.119300).
- 63 L. Cao, Y. Wang, Q. Zhu, L. Fan, Y. Wu, Z. Li, S. Xiong and F. Gu, *ACS Appl. Mater. Interfaces*, 2022, **14**, 17249–17258, DOI: [10.1021/acsami.2c00163](https://doi.org/10.1021/acsami.2c00163).
- 64 P. Yu, L. Wang, F. Sun, Y. Xie, X. Liu, J. Ma, X. Wang, C. Tian, J. Li and H. Fu, *Adv. Mater.*, 2019, **31**, 1901666, DOI: [10.1002/adma.201901666](https://doi.org/10.1002/adma.201901666).
- 65 Y. Li, J. Yin, L. An, M. Lu, K. Sun, Y.-Q. Zhao, D. Gao, F. Cheng and P. Xi, *Small*, 2018, **14**, 1801070, DOI: [10.1002/smll.201801070](https://doi.org/10.1002/smll.201801070).
- 66 Q. Zhang, X. L. Li, B. X. Tao, X. H. Wang, Y. H. Deng, X. Y. Gu, L. J. Li, W. Xiao, N. B. Li and H. Q. Luo, *Appl. Catal., B*, 2019, **254**, 634–646, DOI: [10.1016/j.apcatb.2019.05.035](https://doi.org/10.1016/j.apcatb.2019.05.035).
- 67 L. Wu, J. Li, C. Shi, Y. Li, H. Mi, L. Deng, Q. Zhang, C. He and X. Ren, *J. Mater. Chem. A*, 2022, **10**, 16627–16638, DOI: [10.1039/D2TA03554E](https://doi.org/10.1039/D2TA03554E).
- 68 C. Tang, B. Wang, H.-F. Wang and Q. Zhang, *Adv. Mater.*, 2017, **29**, 1703185, DOI: [10.1002/adma.201703185](https://doi.org/10.1002/adma.201703185).
- 69 D. Lyu, S. Yao, A. Ali, Z. Q. Tian, P. Tsiakaras and P. K. Shen, *Adv. Energy Mater.*, 2021, **11**, 2101249, DOI: [10.1002/aenm.202101249](https://doi.org/10.1002/aenm.202101249).
- 70 N. Radenahmad, R. Khezri, A. A. Mohamad, M. T. Nguyen, T. Yonezawa, A. Somwangthanaroj and S. Kheawhom, *J. Alloys Compd.*, 2021, **883**, 160935, DOI: [10.1016/j.jallcom.2021.160935](https://doi.org/10.1016/j.jallcom.2021.160935).
- 71 A. Wang, C. Zhao, M. Yu and W. Wang, *Appl. Catal., B*, 2021, **281**, 119514, DOI: [10.1016/j.apcatb.2020.119514](https://doi.org/10.1016/j.apcatb.2020.119514).

